communications physics

A Nature Portfolio journal

Article

https://doi.org/10.1038/s42005-026-02533-7

Linked skyrmions in shifted magnetic bilayer

Check for updates

Sumit Ghosh[1,2] ✉, Hiroshi Katsumoto[1], Gustav Bihlmayer[1], Moritz Sallermann[1,3,4], Vladyslav M. Kuchkin[5], Filipp N. Rybakov[6], Olle Eriksson[6], Stefan Blügel[1,3] & Nikolai S. Kiselev[1]

Magnetic solitons have recently attracted significant attention due to their intricate physical properties and potential applications in information processing. The majority of the studies in this field, however, are focused on a particular type of solitons known as skyrmions, characterised by a unit topological charge. Here, we present a shifted magnetic bilayer that can demonstrate magnetic solitons with arbitrary large topological charges. These configurations, which we call *linked skyrmions*, consist of multiple skyrmions linked together with topological point defects. These topological point defects, termed as *anti-aligned* points, originate from the mutually orthogonal Dzyaloshinskii-Moriya interaction in two different layers. By tuning the interlayer exchange coupling and the external magnetic field, one can also achieve different ground states in this bilayer. Additionally, the system also demonstrates conventional *skyrmion-bags* and *kπ*-skyrmions. Finally we propose a suitable material candidate where these magnetic configurations can be realised. Our findings, thus, can provide a way to achieve solitons with large topological charge and realise them in realistic systems.

Magnetic solitons[1,2] are localised magnetic textures which behave like classical particles and can be characterised by a topological index. Their complex mathematical and physical features have stimulated a large number of studies in recent years leading to the discovery of unconventional magnetic texture both in two dimensions[3–6] and three dimensions[7–11]. They can be moved with external charge current[12,13] which makes them a fitting candidate for data storage devices[14–16]. In this regard, the two-dimensional configurations are more promising[17,18] due to their compatibility with current device architectures.

In a condensed matter system, the most common example of magnetic solitons are the *skyrmions*[19,20] which are characterised by an integer topological index. It can be calculated as below for continuous systems,

$$Q = \frac{1}{4\pi}\int dx\, dy\, \mathbf{m}\cdot[\partial_x \mathbf{m}\times\partial_y \mathbf{m}], \tag{1}$$

where $\mathbf{m}$ is the unit vector denoting the magnetisation direction, whereas for discrete systems, the simplicial method applies[21,22]. This is also known as the topological charge of the corresponding magnetic texture or simply the skyrmion charge. While most of the studies are focused on the skyrmions with $|Q|=1$, recently composite skyrmions with arbitrary large topological charge[4,5], commonly known as skyrmion bags, have also been observed experimentally[23–27]. These complex magnetic textures arise from the competition of different magnetic interactions among which the most prominent ones are the Heisenberg exchange and the Dzyaloshinskii-Moriya interaction (DMI)[28,29]. The interplay between these interactions along with an external magnetic field can result in different types of magnetic solitons.

In this paper, we propose a class of complex magnetic solitons with arbitrarily large topological charge which can be realised in a shifted magnetic bilayer. Our model consists of two magnetic layers where the DMI in each layer is mutually perpendicular to each other (Fig. 1). Such a configuration can be achieved by the proximity of a nonmagnetic layer with suitable spin-orbit coupling (SOC). The interlayer coupling can be controlled by using a suitable nonmagnetic spacer. With such anisotropic DMI and an external magnetic field, the proposed bilayer can demonstrate a wide variety of complex solitons along with the existing bag-like skyrmions. By analysing its phase space, we show the suitable parameter region to obtain complex textures with higher topological charges and establish their topological stability with homotopy group analysis. Finally, through a systematic first-principles study, we propose a suitable combination of materials where such complex solitons can be observed.

[1]Peter Grünberg Institut (PGI-1), Forschungszentrum Jülich GmbH, Jülich, Germany. [2]The Institute of Physics of the Czech Academy of Sciences, Prague, Czech Republic. [3]Institute for Theoretical Physics, RWTH Aachen University, Aachen, Germany. [4]Science Institute and Faculty of Physical Sciences, University of Iceland, Reykjavík, Iceland. [5]Department of Physics and Materials Science, University of Luxembourg, Esch-sur-Alzette, Luxembourg. [6]Department of Physics and Astronomy, Uppsala University, Uppsala, Sweden. ✉e-mail: s.ghosh@fz-juelich.de; ghoshs@fzu.cz

Results and discussion

Our system is composed of two magnetic layers made of square lattices (the lattice constant is chosen to be 1) such that the centre of the top and bottom layers are shifted by (1/2, 1/2) (Fig. 1) like a Zincblende structure. A square lattice of nonmagnetic material as a source of SOC is placed such that the centre of this lattice is shifted by (1/2, 0) from the bottom layer and (0, 1/2) from the top layer (Fig. 1). The structural symmetry gives rise to DMI along specific directions only[14,30] as shown in Fig. 1. There might be a small induced DMI in the other direction and along the interlayer bonds which, without loss of generality, is set to zero. For simplicity, we also ignore the effect of any magneto-crystalline anisotropy which does not change the qualitative nature of the outcomes. The direction of the dominant DMI vector ($\boldsymbol{d}_{ij}$) along the line $\boldsymbol{r}_{ij}$ connecting site i and j for top(T) and bottom(B) layers are defined as

$$\boldsymbol{d}_{ij}^{T} = \begin{cases} 0, & \boldsymbol{r}_{ij} \parallel \boldsymbol{e}_x, \\ \boldsymbol{e}_x, & \boldsymbol{r}_{ij} \parallel \boldsymbol{e}_y, \end{cases} \quad \boldsymbol{d}_{ij}^{B} = \begin{cases} -\boldsymbol{e}_y, & \boldsymbol{r}_{ij} \parallel \boldsymbol{e}_x, \\ 0, & \boldsymbol{r}_{ij} \parallel \boldsymbol{e}_y, \end{cases} \tag{2}$$

and the complete lattice magnetic Hamiltonian for the bilayer is given by

$$\begin{aligned} \mathcal{H} \;=\; & -J \sum_{\langle ij\rangle;l} \boldsymbol{m}_i^l \cdot \boldsymbol{m}_j^l - D \sum_{\langle ij\rangle;l} \boldsymbol{d}_{ij}^l \cdot (\boldsymbol{m}_i^l \times \boldsymbol{m}_j^l) \\ & -J_C \sum_{\langle i'j'\rangle} \boldsymbol{m}_{i'}^T \cdot \boldsymbol{m}_{j'}^B - \mu B_{ext} \sum_{i,l} \boldsymbol{e}_z \cdot \boldsymbol{m}_i^l, \end{aligned} \tag{3}$$

where $\langle ij\rangle$ indicates summation over the nearest neighbours in the same layer and $\langle i'j'\rangle$ corresponds to the summation over the nearest neighbours of different layers. The superscript l runs over the top (T) and bottom (B) layer. J and J_C correspond to the Heisenberg exchange parameters within the same and between different layers, respectively, and D is the magnitude of DMI. Here we consider J, $J_C > 0$ resulting in a ferromagnetic coupling and $D = 0.2$ J. We consider the same J, J_C along both x and y direction, which is a valid assumption for $J_C << J$. The model, therefore, can be considered as two mono-axial chiral magnets[31] coupled by the ferromagnetic interlayer exchange (J_C). μ is the onsite magnetic moment and B_{ext} is the external magnetic field applied along z axis.

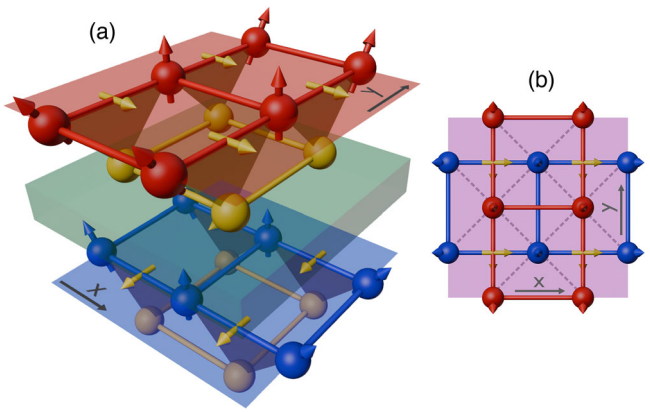

Fig. 1 | Schematic of the shifted magnetic bilayer. a The red, blue and yellow spheres represent the top magnetic, bottom magnetic and non-magnetic sites. The resulting directions of the Dzyaloshinskii-Moriya vectors are shown with yellow arrows. Red and blue arrows show the favourable orientation of the spin due to the Dzyaloshinskii-Moriya interaction. The green region shows the nonmagnetic spacer layer. **b** Top view of the bilayer. The dashed lines show the nearest neighbours from opposite layers.

Phase diagram

The phase diagram of the system is constructed by varying the interlayer coupling J_C and external field B_{ext} (Fig. 2). In the absence of any interlayer coupling ($J_C = 0$) and external magnetic field ($B_{ext} = 0$), the ground state of the system is made of spin spirals with q vector $|\boldsymbol{q}_{B,T}| = D/J$. For our choice of parameters, the optimal wavelength of such a spin spiral is $L_D = 2\pi/|\boldsymbol{q}_L| = 31.5$ which is also reflected in our numerical simulation. When viewed together as a bilayer, the superimposed spirals create a checkerboard pattern and therefore we call this phase *checkerboard* phase (Fig. 2d–f) (Also, see Supplementary Note I). This phase remains the ground state for small J_C ($J_C/J \lesssim 0.01$). It is important to note that here we have the *coexistence* of q-states (layer-by-layer), which should not be confused with the multi-q *approximation* of periodic magnetic textures[32]. The feature that distinguishes this

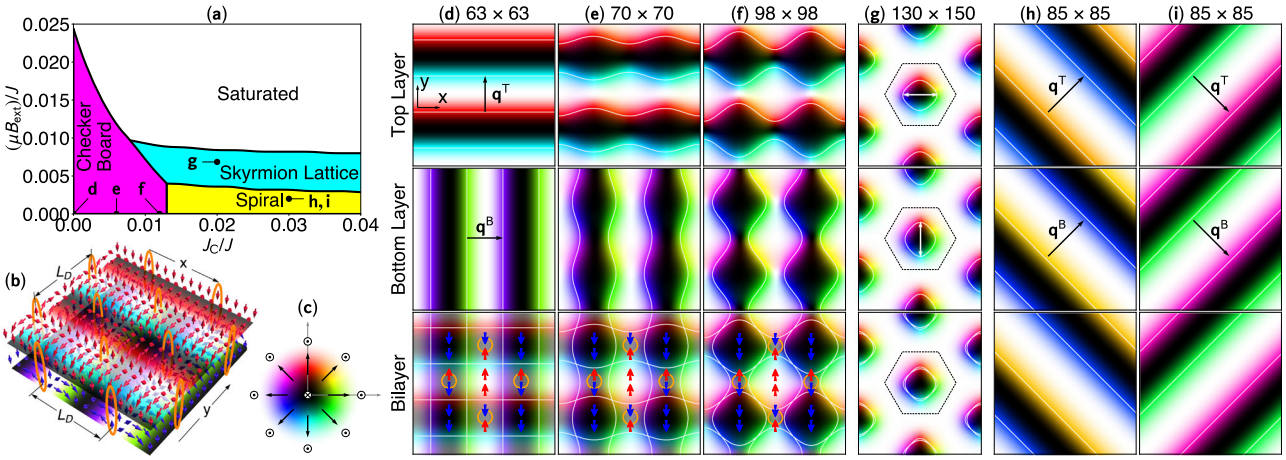

Fig. 2 | Phase diagram and different periodic ground states of the bilayer Hamiltonian (Eq. (3)). a Phase diagram showing checkerboard (magenta), spiral (yellow), skyrmion lattice (cyan), saturated ferromagnetic (white) phase, and the location of the representative configurations. **b** Schematic of the checkerboard in the decoupled limit ($J_C = 0$) and in the absence of the external magnetic field ($B_{ext} = 0$). Orange ellipses show the *anti-aligned* points. **c** Colour code used in the figures demonstrated with an isotropic Néel skyrmion. ⊙ (⊗) shows the region with positive(negative) out of plane components denoted by black(white) colour. Layer resolved checkerboard pattern with $B_{ext} = 0.0$ and **d** $J_C = 0.0$ J, **e** $J_C = 0.006$ J and **f** $J_C = 0.012$ J. $\boldsymbol{q}_{T,B}$ shows the direction of the spiral q vector in top, bottom layer. The numbers on the top show the optimal cell size. White lines show the trajectory of the zero out-of-plane magnetisation. Orange circles show the location of the *anti-aligned* points, and red and blue arrows show the out-of-plane magnetic alignment from the top and bottom layer in the corresponding region. **g** Skyrmion lattice phase obtained at ($J_C = 0.02$ J, $\mu B_{ext} = 0.007$ J). The dashed hexagon denotes the domain of the skyrmion (Eq. (4)) and the white arrows show the elongation of the skyrmion in individual layers. **h**, **i** Show two degenerate spin spiral configurations obtained at ($J_C = 0.03$ J, $\mu B_{ext} = 0.002$ J).

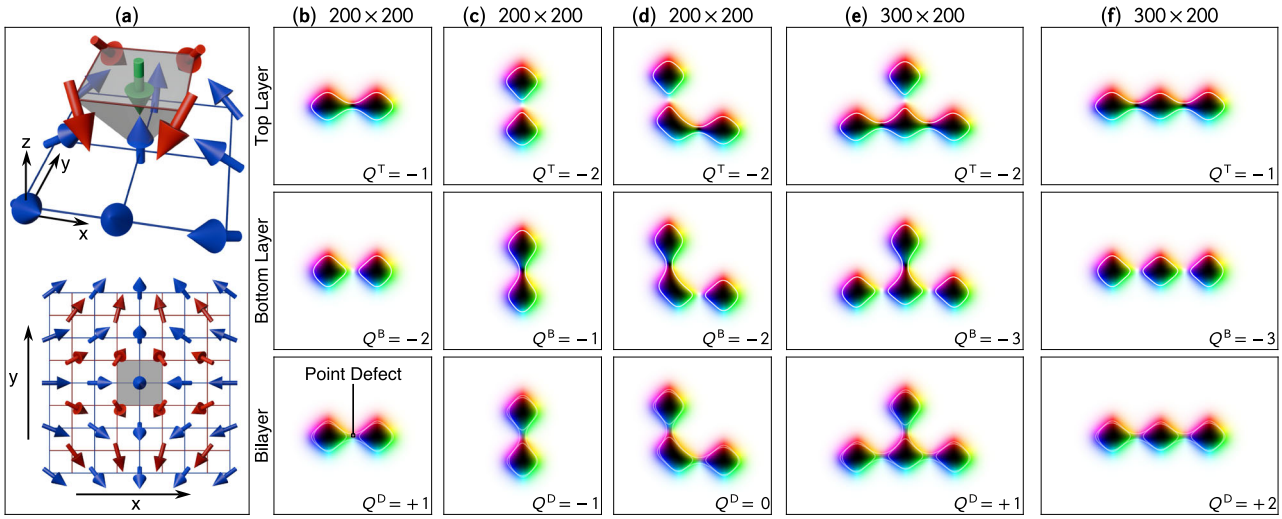

Fig. 3 | Linked skyrmion with different topological charges. a Enlarged view of the topological point defect. The red and blue arrows show the magnetic moment on the top and bottom layers. The green arrow shows the average of the four magnetic moments of the top layer, which constitutes the *anti-aligned* point confined within the grey region. The bottom panel shows the top view of the extended region containing the point defect (region marked by the small square at the bottom panel of column (**b**)), where the grey box denotes the region of the *anti-aligned* point. **b–f** Different linked skyrmions with their topological charge from the top (Q^T) and bottom (Q^B) layers, and the corresponding charge of the topological point defect (Q^D). All configurations are stabilised at ($J_C = 0.02\,J$, $\mu B_{ext} = 0.007\,J$) in a 400 × 400 mesh. The numbers on top denote the dimensions of the plotting regions.

checkerboard phase from the earlier monolayer checkerboard configuration formed by multi-q spin waves[33], is the presence of points where the top and bottom layers are aligned against the direction favoured by the interlayer exchange (marked by orange circles in Fig. 2b, d–f). We call these points *anti-aligned* points. In the subsection *Linked skyrmion*, we show that these points can be characterised as topological defects which play a crucial role in the formation of *linked skyrmions*, a configuration where multiple skyrmions are *linked* together by such topological point defects. With the increase of interlayer coupling, such points become less favourable and the ground state is made of spin spirals where the $(\boldsymbol{q}_T \to \boldsymbol{q}_B)||\boldsymbol{e}_x \pm \boldsymbol{e}_y$. With the increase of the external magnetic field, the ground state is gradually transformed into a skyrmion lattice. Note that, due to the anisotropic DMI, skyrmions in each layer have a small elongation (marked by white arrows in Fig. 2g). As a result the skyrmions and therefore the skyrmion lattice itself possess a two-fold rotation symmetry, rather than conventional six fold rotation symmetry observed in a hexagonal skyrmion lattice[32,34]. Unlike the checkerboard or the spiral phase, the skyrmion lattice phase can be characterised by a non-zero topological charge (Eq. (1)) where the skyrmion domain is the unit cell of the lattice (denoted by the dashed line in Fig. 2g). For convenience, we define a layer-resolved topological charge with representative formulas for the continuum limit

$$Q_{T,B} = \frac{1}{4\pi}\int dx\,dy\,\mathbf{m}^{T,B}\cdot[\partial_x\mathbf{m}^{T,B}\times\partial_y\mathbf{m}^{T,B}], \tag{4}$$

while for our discrete problem, we calculate the $Q_{T,B}$ values accordingly using the Berg-Lüscher simplicial method[21]. In case of the skyrmion lattice, the integration is done over a finite region marked by the dashed line in ref. Fig. 2g which gives $Q_T = Q_B = -1$.

Along with the skyrmion lattice, a large variety of complex metastable states with arbitrarily large topological charges can also coexist within the same parameter region. These states are broadly classified into two classes–(i) Linked skyrmions and (ii) Skyrmion bags and kπ-skyrmions. In case of a linked skyrmion one can have both $Q_T \neq Q_B$ and $Q_T = Q_B$ with one or multiple point defect whereas for the kπ-skyrmion and skyrmion bags always have $Q_T = Q_B$ and no point defect. These are elaborated in the subsections *Linked skyrmion* and *Skyrmion bags and kπ-skyrmions*

Linked skyrmion

The transition from the checkerboard phase to the skyrmion lattice phase is achieved by increasing the interlayer coupling and applying an external field. This makes the *anti-aligned* points energetically unfavourable. However, survival of an *anti-aligned* point leads to the formation of a magnetic texture where one can have $Q^T \neq Q^B$ which we call a *linked skyrmion* (Fig. 3). Such configurations are observed over a wide range in the phase space where skyrmion lattice is observed (See Supplementary Note I and II). In Fig. 3 we use $J_C/J = 0.02$ and $\mu B_{ext}/J = 0.007$ which are the same values used to stabilise skyrmion lattice (Fig. 2g). Such textures can have any number of skyrmions in each layer resulting in an arbitrarily large topological charge.

Topological nature of the skyrmion links: At the centre of each skyrmion link, lies an *anti-aligned* point. As a result, the average magnetisation of the bilayer in the surrounding region tends to be zero. Thus, the texture in Fig. 3a can be considered to contain a point defect. Similar to the Bloch point[35]—a magnetic point defect in bulk crystals—the *anti-aligned* points can also be characterised by a topological charge, Q^D which differs from the skyrmion topological charge (see Supplementary Note III). Here, the topological charge of such a point defect can be expressed in terms of the skyrmion topological charges in the top and bottom layers as

$$Q^D = Q^T - Q^B. \tag{5}$$

For the linked-skyrmions, therefore, it is specifically the difference of Q^T and Q^B that serves as a meaningful classifying quantity.

Skyrmion bags and kπ-skyrmions

The other class of configurations present in the same region of the phase space contains textures with $Q^T = Q^B$ and consequently $Q^D = 0$ (Fig. 4). We use $J_C/J = 0.02$ and $\mu B_{ext}/J = 0.007$ for comparing them with skyrmion lattice and linked skyrmions. These textures can be further divided into two subclasses namely skyrmion bags[4,5] and so-called kπ-skyrmions[36]. Note that, unlike the linked skyrmion, here the total topological charge can be both positive or negative as well as zero.

Material realisation

We have conducted a thorough first-principles study to identify a suitable material for this system. Our studies show that the thin-film

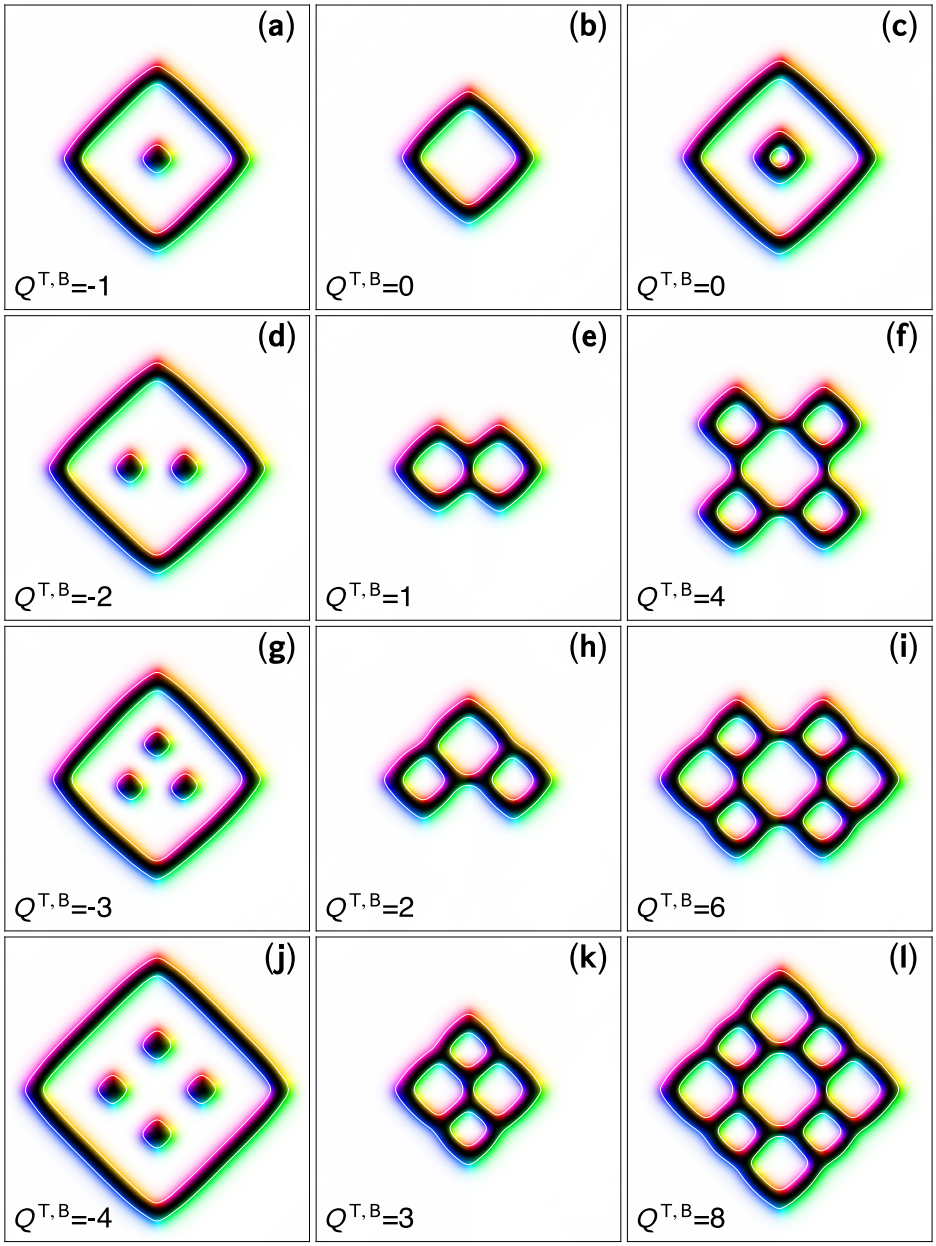

Fig. 4 | Different composite skyrmions without a point defect. a–c $k\pi$-skyrmions and **d–l** skyrmion bags with different topological charges stabilised at ($J_C = 0.02\,J$, $\mu B_{ext} = 0.007J$) in a 400 × 400 mesh. The figures present the total magnetisation of both layers. The legends show the topological charge from the top and bottom layers.

structure of Ni/InAs(001) can be an ideal candidate which possesses all the relevant symmetry and necessary DMI (Fig. 5). The exchange and DMI along x and y direction are obtained from the total energy of the spin spirals with different q vectors (Fig. 5b). Although our calculation shows the existence of finite exchange and DMI beyond the first nearest neighbours (see Supplementary Note IV for details), the dominant contribution comes from the first nearest neighbours. Considering the leading order contribution, for the top layer we find that $J_x = 1.4$ meV, $D_x = 0$ meV and $J_y = 1.6$ meV, $D_y = 0.1$ meV where the suffix denotes the direction of the bond. Due to the symmetry, the bottom layer would have the same magnitude of the J and D parameters with x and y being interchanged. The atomic magnetic moment of Ni is found to be 0.55 μ_B. Our numerical simulations show that with these magnitude of exchange and DMI one can stabilise a linked skyrmion similar to that shown in Fig. 3b with a magnetic field of 70 mT over a wide range of J_C ($0.002 < J_C/J < 0.005$) with a typical dimension of 130 nm × 45 nm.

Conclusion

In this work, we introduce a shifted magnetic bilayer that hosts a wide range of magnetic configurations which can be obtained by tuning the interlayer exchange coupling and an external magnetic field. A characteristic feature of the ground state at weak interlayer coupling and external field is the presence of special regions in which the interlayer magnetic alignment is opposite to the direction favoured by the interlayer exchange. We call these points *anti-aligned* points, which play a crucial role in connecting multiple solitons creating a class of complex magnetic textures with arbitrarily large topological indices, referred to here as *linked skyrmions*. A homotopy group analysis demonstrates that these points are topologically stable. In addition to linked skyrmions, our model also supports conventional $k\pi$-skyrmions and skyrmion bags, which can also host arbitrarily large topological charges. However, linked skyrmions provide a higher topological charge density, which can significantly enhance their transport features, such as a larger effective Hall angle, as well as increased non-linearity of their

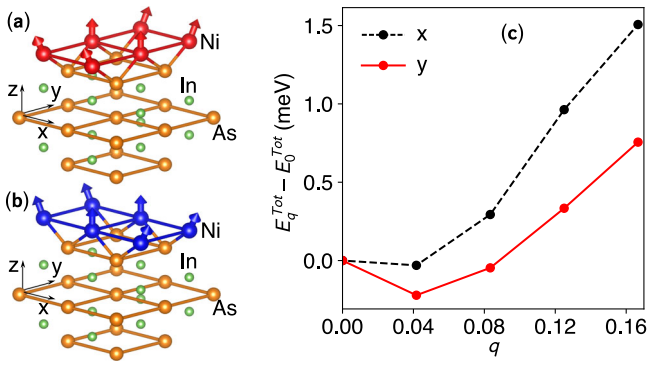

Fig. 5 | Material realisation of the bilayer model. The thin-film structure of the Ni/InAs(001) interface for **a** top and **b** bottom layer. Red and blue spheres denote Ni (magnetic) for the top and bottom layers, and yellow spheres denote In (the main source of SOC). As is shown in green. **c** Total energy of spin spiral for the top layer (**a**), where the red and black dashed lines represent the spiral along *y* and *x* direction on the top layer.

dynamical response. These features make them more promising candidates for skyrmion based computing compared with conventional skyrmions. Finally, based on first-principles calculations, we propose suitable materials in which such solitons can be observed. As a concrete example, we identify a Ni/InAs(001) thin-film system that possesses all required symmetries and interactions. The interlayer coupling can be tuned by controlling the thickness of the InAs layers and also by inserting a suitable non-magnetic spacer layer. Owing to the generality of our theoretical framework, a broad class of materials is expected to satisfy the necessary symmetry conditions to realise these phenomena. Our results therefore provide a route towards engineering higher-order topological solitons in realistic magnetic systems.

Method

Atomistic simulation

The atomistic simulation is done with the atomistic simulation code Spirit[37]. The optimised solutions are obtained by minimising the energy with a convergence threshold of 10^{-10} *J*. In case of periodic configurations shown in Fig. 2d–i the optimum system size is obtained by varying the dimension and finding the dimension corresponding to the minimum energy for each set of parameters. For the isolated solitons (Figs. 3, 4) we use $D = 0.2\,J$, $J_C = 0.02\,J$ and $\mu B_{ext} = 0.007\,J$ and a mesh size of 400 × 400 to avoid finite size effects.

Homotopy-group analysis

Following the approach proposed in ref. 38,39 (See Supplementary Note III for details), we first define an effective space for the order parameter by analysing the most unfavourable spin orientations as

$$X = \{(\boldsymbol{m}^{\mathrm{T}}, \boldsymbol{m}^{\mathrm{B}});\ \boldsymbol{m}^{\mathrm{T}} \in \mathbb{S}^2,\ \boldsymbol{m}^{\mathrm{B}} \in \mathbb{S}^2,\ \boldsymbol{m}^{\mathrm{T}} \neq -\boldsymbol{m}^{\mathrm{B}}\}. \tag{6}$$

Note that X is the homotopy equivalent to $\mathbb{S}^2$. Considering the first homotopy group $\pi_1(X) = \pi_1(\mathbb{S}^2) = 0$, one can see that there are no stable vortices in this system. Each layer can have ordinary skyrmions corresponding to the map $I^2/\partial I^2 \to \mathbb{S}^2$, where I^2 is a rectangle and ∂I^2 is its perimeter. The corresponding topological charges of the skyrmions in each layer are given by

$$Q^L = \frac{1}{4\pi} dS\, \mathbf{F}^L \cdot \hat{e}_z, \tag{7}$$

where $F_z^L = \boldsymbol{m}^{\mathrm{L}} \cdot (\partial_x \boldsymbol{m}^{\mathrm{L}} \times \partial_y \boldsymbol{m}^{\mathrm{L}})$ and L = T, B represents the top and the bottom layers. In addition to that, the system can have stable point defects corresponding to the second homotopy group $\mathbb{S}^2 \to \mathbb{S}^2$, $\pi_2(\mathbb{S}^2) = \mathbb{Z}$. The preimage of the map is a closed surface of containing a point defect (See Fig. 3). The topological charge of this point defect can be defined by the Kronecker integral

$$Q^D = \frac{1}{4\pi} \oiint dS\, \boldsymbol{F} \cdot \hat{\boldsymbol{n}}, \tag{8}$$

where $\hat{\boldsymbol{n}}$ is the unit normal to the surface and $\boldsymbol{F}$ is the vector curvature. For a trapezoidal volume around the point defect, we have $\hat{\boldsymbol{n}}^T = -\hat{\boldsymbol{n}}^B = \hat{e}_z$. Using Eq. (7) and keeping in mind that the net contribution from the side surfaces vanishes, we obtain

$$Q^D = Q^T - Q^B, \tag{9}$$

which represents the topological point defect as the difference of the stable skyrmion topological charges of the individual layers.

First-principles calculations

The first-principles calculations were performed using the ab initio code FLEUR[40]. Here we use a symmetric thin film structure (see Supplementary Note IV for details). By placing a single layer of Ni in a square lattice on top of the (001) plane of InAs, such that the square lattice is shifted by half the lattice vector along the *y* (for top layer, Fig. 5a) or the *x* (for bottom layer, Fig. 5b) axis with respect to the square formed by the adjacent As atoms, the resulting crystal symmetry will produce the same orientation of the D-vectors as shown in Fig. 1. For the structure in Fig. 5, the most stable in-plane lattice constant near the InAs lattice constant was determined (4.268 Å) by relaxation of internal coordinates along the *z*-axis such that the force on each atom is below 10^{-6} Hartree/Bohr. The result shows that the structure remains stable with Ni bound to InAs without detachment. After the structural relaxation, we calculate the energy of the spin spiral using the generalised Bloch theorem[41]. For our calculation we use a 48 × 48 × 1 k-mesh. The total energy for different values of q along x and y axis is shown in Fig. 5b. To obtain J, we calculate the energy of the spin spiral along direction $\hat{i}$ without SOC and fit it with $E(q_i) = E(-q_i) = -E_0 - \sum_n J_i^n \cos(2n\pi q_i)$ where J_i^n is the Heisenberg exchange between n^{th} nearest neighbour along $\hat{i}$. For the DMI we calculate the energy due to SOC and fit it with $E_{SOC}(q_i) = -E_{SOC}(-q_i) = -\sum_n D_i^n \sin(2n\pi q_i)$ where D_i^n is the DMI vector between n^{th} nearest neighbour along $\hat{i}$ direction (see Supplementary Note IV for details).

Data availability

The datasets generated during and/or analysed during the current study are available from the corresponding author on reasonable request.

Received: 27 June 2025; Accepted: 28 January 2026;
Published online: 24 February 2026

References

1. Kosevich, A., Ivanov, B. & Kovalev, A. Magnetic solitons. *Phys. Rep.* **194**, 117–238 (1990).
2. Manton, N. & Sutcliffe, P. *Topological Solitons.* https://www.cambridge.org/core/product/identifier/9780511617034/type/book (Cambridge University Press, 2004).
3. Lin, S.-Z., Saxena, A. & Batista, C. D. Skyrmion fractionalization and merons in chiral magnets with easy-plane anisotropy. *Phys. Rev. B* **91**, 224407 (2015).
4. Foster, D. et al. Two-dimensional skyrmion bags in liquid crystals and ferromagnets. *Nat. Phys.* **15**, 655–659 (2019).
5. Rybakov, F. N. & Kiselev, N. S. Chiral magnetic skyrmions with arbitrary topological charge. *Phys. Rev. B* **99**, 064437 (2019).
6. Göbel, B., Mertig, I. & Tretiakov, O. A. Beyond skyrmions: review and perspectives of alternative magnetic quasiparticles. *Phys. Rep.* **895**, 1–28 (2021).

7. Okumura, S., Hayami, S., Kato, Y. & Motome, Y. Magnetic hedgehog lattices in noncentrosymmetric metals. *Phys. Rev. B* **101**, 144416 (2020).
8. Kent, N. et al. Creation and observation of hopfions in magnetic multilayer systems. *Nat. Commun*. **12**, https://doi.org/10.1038/s41467-021-21846-5 (2021).
9. Azhar, M., Kravchuk, V. P. & Garst, M. Screw dislocations in chiral magnets. *Phys. Rev. Lett.* **128**, 157204 (2022).
10. Zheng, F. et al. Hopfion rings in a cubic chiral magnet. *Nature* **623**, 718–723 (2023).
11. Liu, Y. & Nagaosa, N. Current-induced creation of topological vortex rings in a magnetic nanocylinder. *Phys. Rev. Lett.* **132**, 126701 (2024).
12. Woo, S. et al. Observation of room-temperature magnetic skyrmions and their current-driven dynamics in ultrathin metallic ferromagnets. *Nat. Mater.* **15**, 501–506 (2016).
13. Wang, X. S., Qaiumzadeh, A. & Brataas, A. Current-driven dynamics of magnetic hopfions. *Phys. Rev. Lett.* **123**, 147203 (2019).
14. Fert, A., Cros, V. & Sampaio, J. Skyrmions on the track. *Nat. Nanotechnol.* **8**, 152–156 (2013).
15. Yu, G. et al. Room-temperature skyrmion shift device for memory application. *Nano Lett.* **17**, 261–268 (2016).
16. He, B. et al. All-electrical 9-bit skyrmion-based racetrack memory designed with laser irradiation. *Nano Lett.* **23**, 9482–9490 (2023).
17. Fert, A., Reyren, N. & Cros, V. Magnetic skyrmions: advances in physics and potential applications. *Nat. Rev. Mater.* **2**, 17031 (2017).
18. Everschor-Sitte, K., Masell, J., Reeve, R. M. & Kläui, M. Perspective: magnetic skyrmions - Overview of recent progress in an active research field. *J. Appl. Phys*. **124**, 240901 (2018).
19. Rößler, U. K., Bogdanov, A. N. & Pfleiderer, C. Spontaneous skyrmion ground states in magnetic metals. *Nature* **442**, 797–801 (2006).
20. Nagaosa, N. & Tokura, Y. Topological properties and dynamics of magnetic skyrmions. *Nat. Nanotechnol.* **8**, 899–911 (2013).
21. Berg, B. & Lüscher, M. Definition and statistical distributions of a topological number in the lattice o(3) σ-model. *Nucl. Phys. B* **190**, 412–424 (1981).
22. Outerelo, E. & Ruiz, J. M. *Mapping degree theory*. Graduate Studies in Mathematics, Vol. 108 (American Mathematical Society Providence, 2009).
23. Tang, J. et al. Magnetic skyrmion bundles and their current-driven dynamics. *Nat. Nanotechnol.* **16**, 1086–1091 (2021).
24. Powalla, L. et al. Seeding and emergence of composite skyrmions in a van der Waals magnet. *Adv. Mater.* **35**, 2208930 (2023).
25. Zhang, Y. et al. Stable skyrmion bundles at room temperature and zero magnetic field in a chiral magnet. *Nat. Commun.* **15**, 3391 (2024).
26. Yang, L. et al. Embedded skyrmion bags in thin films of chiral magnets. *Adv. Mater.* **2403274**, 1–10 (2024).
27. Hassan, M. et al. Dipolar skyrmions and antiskyrmions of arbitrary topological charge at room temperature. *Nat. Phys.* **20**, 615–622 (2024).
28. Dzialoshinskii, I. E. Thermodynamical theory of weak ferromagnetism in antiferromagnetic substances. *JETP* **5**, 1259–1272 (1957).
29. Moriya, T. Anisotropic superexchange interaction and weak ferromagnetism. *Phys. Rev.* **120**, 91–98 (1960).
30. Fert, A. & Levy, P. M. Role of anisotropic exchange interactions in determining the properties of spin-glasses. *Phys. Rev. Lett.* **44**, 1538–1541 (1980).
31. Kishine, J.-i. & Ovchinnikov, A. *Theory of Monoaxial Chiral Helimagnet* 1–130 https://doi.org/10.1016/bs.ssp.2015.05.001 (Elsevier, 2015).
32. Okubo, T., Chung, S. & Kawamura, H. Multiple-q states and the skyrmion lattice of the triangular-lattice heisenberg antiferromagnet under magnetic fields. *Phys. Rev. Lett.* **108**, 017206 (2012).
33. Hayami, S. Checkerboard bubble lattice formed by octuple-period quadruple-q spin density waves. *Phys. Rev. B* **108**, 094415 (2023).
34. Mühlbauer, S. et al. Skyrmion lattice in a chiral magnet. *Science* **323**, 915–919 (2009).
35. Malozemoff, A. P. & Slonczewski, J. C. *Magnetic Domain Walls in Bubble Materials: Advances in Materials and Device Research* (Academic Press, 1979).
36. Bogdanov, A. & Hubert, A. The stability of vortex-like structures in uniaxial ferromagnets. *J. Magn. Magn. Mater.* **195**, 182–192 (1999).
37. Müller, G. P. et al. Spirit: multifunctional framework for atomistic spin simulations. *Phys. Rev. B* **99**, 224414 (2019).
38. Rybakov, F. N. & Eriksson, O. Non-abelian vortices in magnets. *preprint arXiv*. https://arxiv.org/abs/2205.15264 (2022).
39. Rybakov, F. N., Eriksson, O. & Kiselev, N. S. Topological invariants of vortices, merons, skyrmions, and their combinations in continuous and discrete systems. *Phys. Rev. B* **111**, 134417 (2025).
40. The FLEUR project. https://www.flapw.de/.
41. Heide, M., Bihlmayer, G. & Blügel, S. Describing Dzyaloshinskii-Moriya spirals from first principles. *Phys. B* **404**, 2678–2683 (2009).
42. Thörnig, P. JURECA: data centric and booster modules implementing the modular supercomputing architecture at jülich supercomputing centre. *J. Large Scale Res. Facil.* **7**, A182–A182 (2021).

Acknowledgements

S.G. is co-funded by the European Union (Physics for Future—Grant Agreement No. 101081515). This work is supported by the Ministry of Education, Youth and Sports of the Czech Republic through the e-INFRA CZ (ID:90254). This project has received funding from the European Research Council under the European Union's Horizon 2020 Research and Innovation Programme (Grant No. 856538—project "3D MAGiC"). H.K. acknowledges computing time on the supercomputer JURECA[42] at Forschungszentrum Jülich under grant no. JIFF38. F.N.R. and O.E. acknowledge support from the Swedish Research Council (Grant No. 2023-04899).

Author contributions

S.G., H.K. and S.B. have initiated the project. S.G. has established the model and obtained different solutions. H.K. has conducted the symmetry analysis, identified suitable material candidate and carried out the first-principles calculation with G.B. F.N.R has carried out the homotopy group analysis. M.S. has helped with the atomistic simulation. V.K. has helped with the phase diagram. S.B., O.E. and N.S.K. have contributed in analysing the results. S.G. has written the manuscript with feedback from others. All co-authors have discussed the results and contributed equally.

Funding

Open Access funding enabled and organized by Projekt DEAL.

Competing interests

The authors declare no competing interests.

Additional information

Supplementary information The online version contains supplementary material available at https://doi.org/10.1038/s42005-026-02533-7.

Correspondence and requests for materials should be addressed to Sumit Ghosh.

Peer review information *Communications Physics* thanks Zukhra Gareeva, Xiansi Wang and the other, anonymous, reviewer(s) for their contribution to the peer review of this work. [A peer review file is available].

Reprints and permissions information is available at http://www.nature.com/reprints

Publisher's note Springer Nature remains neutral with regard to jurisdictional claims in published maps and institutional affiliations.

Open Access This article is licensed under a Creative Commons Attribution 4.0 International License, which permits use, sharing, adaptation, distribution and reproduction in any medium or format, as long as you give appropriate credit to the original author(s) and the source, provide a link to the Creative Commons licence, and indicate if changes were made. The images or other third party material in this article are included in the article's Creative Commons licence, unless indicated otherwise in a credit line to the material. If material is not included in the article's Creative Commons licence and your intended use is not permitted by statutory regulation or exceeds the permitted use, you will need to obtain permission directly from the copyright holder. To view a copy of this licence, visit http://creativecommons.org/licenses/by/4.0/.

© The Author(s) 2026